Earth and Planetary Science Letters 491 (2018) 244–254

Contents lists available at ScienceDirect

Earth and Planetary Science Letters

www.elsevier.com/locate/epsl

First detection of precursory ground inflation of a small phreatic eruption by InSAR

Tomokazu Kobayashi *, Yu Morishita, Hiroshi Munekane

Geospatial Information Authority of Japan, Kitasato-1, Tsukuba, Ibaraki 305-0811, Japan

ARTICLE INFO

Article history:
Received 31 December 2017
Received in revised form 6 March 2018
Accepted 16 March 2018
Available online 6 April 2018
Editor: J.-P. Avouac

Keywords:
precursory ground inflation
phreatic eruption
SAR
Hakone-Owakudani

ABSTRACT

Phreatic eruptions are caused by pressurization of geothermal fluid sources at shallow levels. They are relatively small compared to typical magmatic eruptions, but can be very hazardous. However, owing to their small magnitudes, their occurrences are difficult to predict. Here we show the detection of locally distributed ground inflation preceding a small phreatic eruption at the Hakone volcano, Japan, through the application of interferometric synthetic aperture radar analysis. The ground inflation proceeded the eruption at slow speed of ~5 mm/month with a spatial size of ~200 m in the early stage, and then it accelerated 2 months before the eruption that occurred for the first time in 800–900 yrs. The ground uplift reached ~30 cm, and the eruption occurred nearby the most deformed part. The deformation speed correlated well with inflation of spherical source located at 4.8 km below sea level, thus suggesting that heat and/or volcanic fluid supply from the spherical source, maybe magma reservoir, directly drove the subsurface hydrothermal activity. Our results demonstrate that high-spatial-resolution deformation data can be a good indicator of subsurface pressure conditions with pinpoint spatial accuracy during the preparatory process of phreatic eruptions.

1. Introduction

Phreatic eruptions are thought to be related to transient pressure changes in subsurface hydrothermal systems that can be attributed to the heating of shallow aquifers (e.g., Barberi et al., 1992; Germanovich and Lowell, 1995). Crustal deformation presumably proceeds in association with the internal pressure increase during the preparatory process of an eruption in the proximity of future vent, which would be a useful precursory signal to infer the potential area of eruption start if it could be detected. Phreatic eruptions generally take on a wide range of size; some events could be so large that they have serious effects on distant areas such as the 1980 eruption of Mount St. Helens followed by magmatic eruptions (volcanic explosivity index (VEI) = 5) (Shimkin, 1993), others only affect a limited area surrounding the explosive vents such as the 2014 eruption of Mount Ontake, Japan (VEI = 2) (Kato et al., 2015). However, even if the scale is small, phreatic eruptions can be dangerous events, as evidenced by the numerous casualties following the 1990 Agua Shuca eruption in El Salvador; 25 deaths (Handal and Barrios, 2004) and the 2014 Ontake eruption in Japan; 58 deaths (Kato et al., 2015).

One of the difficulties in monitoring phreatic eruptions is that the precursory signals are generally thought to be small and localized (e.g., Barberi et al., 1992). In some cases, precursory signals have been detected for small phreatic eruptions by using seismic and GNSS data (Kato et al., 2015; Miyaoka and Takagi, 2016), which demonstrate that they can be good monitoring approaches to detect anomalous activities prior to an eruption. However, it is difficult to infer the potential area of eruption start with pinpoint spatial accuracy by these types of observations. This is why there are scarce reports of precursor detection to identify potential vents of forthcoming eruption although there has been reports on detection of some types of precursory signals. To enable more effective proactive monitoring, studies on the occurrence potential of future phreatic eruptions are needed.

Mt. Hakone is a caldera volcano with a size of 8 km in the east–west direction and 12 km in the north–south direction (Fig. 1a). The most recent magmatic eruption occurred roughly 3 ka (Kobayashi, 1999), and the last historical eruption, which occurred around the 12th and 13th centuries, was of the phreatomagmatic type (Kobayashi et al., 2006). Several fumarolic activity areas are located within the caldera, and Owakudani (OWK) is one of the most active geothermal areas in this region. In 2015, a small but evident phreatic eruption occurred at OWK on 29–30 June (the exact eruption start time is unknown), which is the first eruption in over 800–900 yrs. This eruption formed

* Corresponding author.
E-mail address: kobayashi-t96dv@mlit.go.jp (T. Kobayashi).

https://doi.org/10.1016/j.epsl.2018.03.041

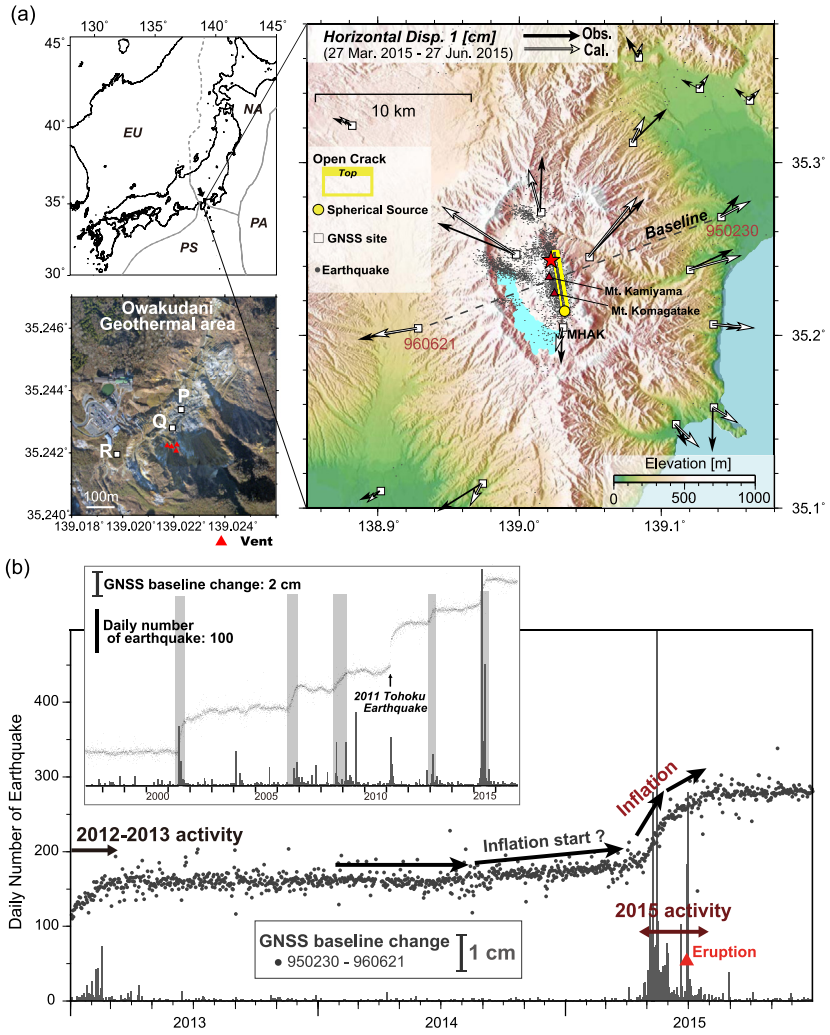

Fig. 1. Hakone volcano and 2015 volcanic activity. (a) Black and white vectors on the map represent the GNSS-derived horizontal ground displacements (27 Mar. 2015 to 27 Jun. 2015) and the model-calculated displacements, respectively. Gray dots are epicenters of earthquake swarms (1 Jan. 2014 to 31 Dec. 2015). The yellow circle and rectangular represent the spherical pressure source and dike opening model, respectively. The red star indicates the Owakudani geothermal area. Left-top and -bottom show the locations of the Hakone volcano within the tectonic setting and an aerial photo of the Owakudani area, respectively. (b) Baseline changes between GNSS stations and seismicity. Dots indicate baseline changes between the 950230 and 960621 stations, respectively. The histogram shows the daily number of earthquakes. The inset shows the baseline changes and the seismicity since 1997. Shaded zones indicate the periods in which GNSS baseline changes and seismic swarms were observed. (For interpretation of the colors in the figure(s), the reader is referred to the web version of this article.)

several vents with diameters of ~20 m, from which volcanic ash consisting of non-juvenile material was erupted in amounts of 40 to 130 tons; the plume height was ~100 to 800 m (Coordinating Committee for Prediction of Volcanic Eruption, 2015).

Several anomalies were observed prior to the 2015 eruption. A seismic swarm started around 26 April 2015, whose hypocenters ran linearly in an almost north–south direction with some branches in the WNW–ESE direction (Fig. 1). The GNSS (Global Navigation Satellite System)-observed horizontal displacements were oriented radially and outwardly, which is suggestive of inflation of the volcano body (Fig. 1a). The GNSS-recorded daily baseline plots show that the distance between the stations started to lengthen in April, and this continued through the eruption at the end of June and finally terminated around August (Fig. 1b). However, it is difficult to use the seismic and GNSS observations to directly measure the ground displacement just above the subsurface hydrothermal system at OWK and to describe the pressure conditions. By contrast, a synthetic aperture radar interferometry (InSAR) is capable of spatially detailed mapping of crustal deformation, which can provide information on the subsurface pressure condition even for a local phenomenon. This study demonstrates that high-spatial-resolution radar satellite data can contribute to the retrieval of locally distributed precursory pressure changes.

2. Data and methods

2.1. InSAR analysis

An L-band synthetic aperture radar (SAR) satellite, known as the Advanced Land Observing Satellite 2 (ALOS-2), collected observations for the 2015 activity. We examined the crustal deformation in OWK before the eruption by SAR interferometry (InSAR) analysis. The analyzed SAR data are listed in Supplementary Table S1. The ALOS-2 data were processed using GSISAR software (Fujiwara and Tobita, 1999; Fujiwara et al., 1999; Tobita et al., 1999; Tobita, 2003) for InSAR processing. We applied multi-look processing with 4 by 4 looks in both the range and azimuth directions, which resulted in pixel spacing of about 5.6 m and 7.2 m in the radar coordinate, respectively. We reduced the atmosphere-related noise using a numerical weather model for the InSAR data (Kobayashi et al., 2014; Kobayashi, 2016).

2.2. Multi-temporal InSAR

As shown later, we could not detect significant ground deformation before the end of April by the standard InSAR analyses. To further confirm the ground deformation before the end of April, we apply a multi-temporal InSAR (MTI) analysis that enables us to measure the temporal evolution of the slowly proceeding deformation. Unfortunately, there were only a few ALOS-2 images available for this task, and thus, we utilized RADARSAT-2 (RS2) and Sentinel-1A (S1) SAR satellites, which acquired ∼10 images every ∼1 month from the end of 2014 to the end of April in 2015 (Supplementary Tables S2 and S3).

To achieve high measurement accuracy in the MTI analysis, in general, use of a persistent scatterer (PS) is robust and efficient. A PS is a coherent radar target, which often corresponds to a point scatter such as a man-made structure. The phase stability is high over time, and thus, a PS can be a suitable measurement point to trace temporal variation on deformation with high measurement accuracy (Ferretti et al., 2001). However, there exist few PS points in mountainous areas unlike in urban areas. This is a critical drawback for monitoring the crustal deformation associated with volcanic activity. Further, to make matters worse, both the RS2 and S1 satellites illuminate C-band microwaves that hinder the ability of InSAR analysis to measure ground displacement in non-urban areas unlike L-band data due to less coherence. Thus, the use of distributed scatterers (DSs), which are pixels that share similar reflectivity values in a resolution cell (Hanssen, 2001) and are dominantly distributed in SAR imagery; unlike a PS that consists of a point-wise bright scatterer, is indispensable for improving the spatial density of measurement points in non-urban areas.

One of the difficult points for the use of DSs is the temporal instability of phase estimates. The phase of a DS, unlike a PS for which the phase is deterministic, can be described by statistical terms (e.g., Bamler and Hartl, 1998; Hanssen, 2001). The phase is dominated by stochastic behaviors, and thus, the multi-looked phases are not linked among all pairs of interferograms (Ferretti et al., 2011). Hence, to make use of the DSs with high measurement accuracy in time series analysis, we have to optimize the phase time series data by some sophisticated approach. In this context, a phase optimization of DS pixels was inevitable to overcome this drawback for the MTI analysis.

Here we basically follow the approach proposed by Ferretti et al. (2011), but partly employ different methods. The basic analysis flow consists of (1) adaptive space filtering for extraction of brother pixels (BPs) (Ferretti et al., 2011), (2) calculation of the complex coherence matrix, and (3) optimization of phase time series data by the maximum likelihood approach under a complex circular Gaussian distribution.

The complex coherence plays an essential role in optimizing the phase history data of DSs during the processing step (3). Estimate of the coherence matrix theoretically requires an ensemble of samples that meet ergodicity (Hanssen, 2001). To reduce the estimate error, multi-looking transactions using only same scatterers should be done to keep the ergodicity. However, the selection of samples by using a conventional simple rectangular estimation window possesses the risk of overestimating/underestimating the coherence because effects of different backscattering characteristics are included with high probability. Thus, to estimate the coherence value with high accuracy, it is necessary to identify groups of neighboring pixels that have similar backscattering characteristics. Ferretti et al. (2011) have proposed an effective way, in which the BPs are extracted by using a Kolmogrov–Smirnov (KS) test, which is a non-parameteric test. The KS test tends to be most sensitive around the median value, while it is less sensitive to deviations at the tails of a probability distribution. To overcome this drawback, some modified KS tests have been proposed. Here, we use Kuiper's test, which is one type of modified KS test, as a relatively simple and numerically easy way of handling owing to the approximate formulation for the probability estimate (Press et al., 1992). This kind of space adaptive filtering represents a multi-look approach, and it has an advantage in that it can preserve point-wise phase information unlike conventional multi-look algorithms (Curlander and McDonough, 1991). Here, we set an estimation window with the size of 11 pixels ×11 pixels and searched BPs within the window.

Once we obtain multi-looked SAR images using the BPs, we can then calculate a complex coherence matrix for all InSAR pairs by using the SAR data obtained from the space adaptive filtering. After obtaining the complex coherence matrix, we retrieve the optimal phase history data of each DS pixel. To get the optimized phases, we used a phase linking algorithm proposed by Guarnieri and Tebaldini (2008). In this algorithm, the optimized phases are obtained as a maximum likelihood estimator assuming a complex circular Gaussian distribution by which the statistical behavior of a DS is described. The joint probability density function (pdf) for the stacked interferometric phases is written as (Ferretti et al., 2001; Zan and Rocca, 2005)

$$\mathrm{pdf}(\mathbf{d} \mid \boldsymbol{\varphi}) \propto \prod \exp\left(-\mathbf{d}^{\mathrm{H}}\mathbf{C}^{-1}\mathbf{d}\right), \tag{1}$$

where $\mathbf{d} = [d_0(x), \cdots, d_{N-1}(x)]^{\mathrm{T}}$ is a complex data vector that consists of $d_i(x)$. The superscript T stands for transpose, and $d_i(x)$ is the complex reflectivity value of the i-th SAR image at pixel x. The superscript H stands for Hermitian transposition. φ_k is the interferometric phase of the k-th acquisition. $\mathbf{C}^{-1}$ is an inverse matrix of the covariance matrix. By solving equation (1), we eventually obtain the following function:

$$\mathrm{F}(\varphi_1, \cdots, \varphi_{N-1}) = \boldsymbol{\xi}^{\mathrm{H}}\left(\boldsymbol{\Gamma}^{-1} \circ \mathbf{I}\right)\boldsymbol{\xi}. \tag{2}$$

Here, $\boldsymbol{\xi}^{\mathrm{H}} = [1, \exp(j\varphi_1), \cdots, \exp(j\varphi_{N-1})]$, and $\mathbf{I}$ is a matrix that consists of all the interferograms. $\circ$ represents the Hadamard product. The maximum likelihood estimate of the interferometric phases is yielded eventually by maximizing the above function.

The phase time series at each pixel is optimized on the basis of coherence information by using all the "wrapped" interferograms. The joint approach combining the space adaptive filter and the phase linking method is more effective than the Small Baseline Subset (SBAS) technique (Berardino et al., 2002) in that the phases are optimized before unwrapping.

By completing the above phase optimization, we can handle the temporally coherent signals that are identical to PS points and incorporate the data into a conventional persistent scatterer interferometry (PSI) (Ferretti et al., 2001) analysis chain. We used a 10-m-mesh digital elevation model (DEM) released by Geospatial Information Authority of Japan (https://fgd.gsi.go.jp/download/ref_dem.html) in the processing. The optimized pixels are used for the PSI analysis in which a linear trend and DEM correction terms are modeled from the time series data. The atmosphere-related noise is reduced by using a numerical weather model (Kobayashi et al., 2014; Kobayashi, 2016). The residual data following subtraction of the modeled DEM error and the modeled atmospheric noise from the original data are regarded as the temporal variation of ground deformation, which consists of linear and non-linear ground deformation, and unmodeled noise. For the PSI analysis, we basically employed the GAMMA/IPTA module (Wegmüller and Werner, 1997; Werner et al., 2003).

Both RS2 and S1 satellites produce C-band SAR data, and thus, coherence is worse than that for L-band data derived from the InSAR method. The coherence in the InSAR results are degraded since May in 2015. To avoid a no-measurement-point spread situation in the central part of the deformation area, we used only

the data acquired before April for the MTI analysis, although there were several available images acquired after April 2015.

3. Result

3.1. InSAR-detected precursory local ground inflation

Fig. 2 shows the time series of the InSAR images. No significant change can be identified until 17 April (Fig. 2a-1, a-2), but line-of-sight (LOS) shortening signals can be clearly recognized from the date of 7 May and onward (Fig. 2b-1). The temporal timing was almost concordant with the appearance of seismicity anomalies and volcano inflation. The deformed area was approximately circular with a diameter of ∼200 m, and the spatial extent did not change throughout the activity. The maximum displacement was positioned at the center of the deformed area in the initial stage (Fig. 2b-1), but the peak location shifted to the southwest starting in the middle of May (Fig. 2a-3, b-2). The LOS shortening signals could be identified from both the ascending and descending orbits of the right-looking mode, which suggests that the uplift was predominant compared to horizontal deformation. The ground inflation evolved with time toward the eruption, but the deformation speed significantly decreased in June (Fig. 2c). A large inflation was observed again in association with the eruptions (Fig. 2a-6, b-5), although it is unclear whether this inflation occurred before or after the eruption.

Assuming that the deformation was sufficiently small in June (Fig. 2a-5, b-4), we estimated the quasi-up–down and -east–west components by using the cumulative LOS displacements (Fig. 3) (Fujiwara et al., 2000). The ground uplift reached approximately 30 cm, and eastward movement was predominant at ∼15 cm at most. The ground was asymmetrically uplifted with maximum displacement in the southwestern most area, as if a lid had opened with a hinge fixed at the northeast. Some surface cracks were observed at the highly-deformed area on 27 May (Hot Springs Research Institute of Kanagawa Prefecture, 2015). The deformation pattern looks like a trapdoor faulting (Amelung et al., 2000).

Here, we stress that the eruption initiated in close proximity to observed deformation area, and the vents in this area are indicated by red triangles in Fig. 2 and 3. Further, it is noteworthy that the vents were located in proximity to the maximum ground uplift area, that is, the eruption started at the most pressurized side within the deformation area. The large deformation associated with the eruption (Fig. 2a-6, b-5) may reflect the rebuilt pressure just before the eruption. The most deformed area would have been subjected to strong extensional strain, where the effective tensile strength of rock should have decreased, thus implying that the southern part of the deformation area enhanced the occurrence potential of the eruption.

Conventional ground-based observations are not available at a spatial density that samples the displacement area associated with such a local and small phreatic eruption, whereas, thanks to the high-spatial-resolution ALOS-2 data, the detailed pressure distribution can be unveiled with pinpoint accuracy. Although ground inflation has been expected to precede a phreatic eruption theoretically (Germanovich and Lowell, 1995), as far as we know, no observational work has detected the spatial distribution and time evolution of such an event. Here, we present the first observational work that succeeded in detecting this kind of precursory signal for a phreatic eruption point. The results thus demonstrate that InSAR-based ground deformation can be a good indicator for proactively knowing the preparatory process of phreatic eruptions.

3.2. Slowly progressive ground deformation in the early preparatory stage

The subsurface pressurization process was almost synchronized with the start of the seismic and GNSS observation anomalies, which allows us to infer that the inflow of magmatic fluids kicked off the subsurface pressure increase at the end of April. Although there were no remarkable anomalous activities before April 2015, we found that the GNSS-derived baseline slightly lengthened starting around the time of August 2014 (Fig. 1b). It is interesting to examine whether or not the ground inflation proceeded at OWK before April 2015 in synchrony with the small baseline change. To characterize the displacement history before the end of April, we apply an MTI analysis that enables us to measure the temporal evolution of the slowly proceeding deformation.

Fig. 4a shows the velocity field estimated by applying the technique to RS2 data. Green-colored pixels, which represent little ground movement, were spread over the analysis domain, but in OWK, we can clearly identify the LOS shortening signal. Fig. 4b shows the time series of InSAR images with reference to 28 September 2014, and these results clearly show that the deformation evolved with time. The ground displacement reached up to ∼3 cm during these six months. The spatial extent of the deformation was approximately circular with a diameter of ∼200 m. The most striking point is that the position and the spatial extent was just the same as that observed by ALOS-2 InSAR since May in 2015 (Fig. 2b-1). The results demonstrate that the locally distributed ground deformation had already started before the outstanding anomalous activity at the end of April 2015.

Similar results were also obtained when using S1 data (Supplementary Fig. S1). The LOS shortening signals could be identified with almost the same spatial extent and location as the RS2-derived deformation. The time histories also had similar features, although the data dispersion was larger than that for the RS2 results (Supplementary Fig. S2).

Although we cannot confirm the component of the movement because only one sight direction was available, the signal probably shows the ground inflation. The phase change area had a northwest-facing slope, and thus, if the ground had landslide-wise movement, the phase change should show the LOS lengthening because both the northwestward movement and subsidence is identical to displacement away from the satellite for the emitting-beam configuration. Thus, the observed displacement was inferred to consist of uplift predominantly as observed by ALOS-2.

Fig. 5 shows the time series data of cumulative LOS displacements, as indicated by circles (RS2) and squares (ALOS-2). The incidence angles of both types of satellite data were almost the same, and thus, the obtained phase changes were comparable given the same time histories. The red and blue lines represent the time histories at points P and Q, which are positioned at the central part and the southern part in the deformed area, respectively (Fig. 4b-7). We here simply connected the time histories of RS2 and ALOS-2 data under the assumption that there was no significant ground displacement between the acquisition dates of master images of RS2 and ALOS-2 (11 days). We can obviously find that the ground slightly but steadily inflated with time at an almost the constant speed; the rate was ∼5 mm/month in the early stage, and then, it accelerated up to almost the same time as the start of the seismic swarm observed at the end of April in 2015. The inset shows the enlargement view of the time histories for RS2. The area within five pixels surrounding points P and Q, as indicated by dotted lines, also systematically moved toward the satellite with a similar speed. The derived time histories of displacements are uncorrelated with those of perpendicular baselines which produces elevation-correlated phase changes, that is, the time evolution of LOS shortening is not produced by the error of the DEM correction estimate. We found that the ground movement could be recognized as significant by the end of 2014 at the latest, although this was not so clear because there were no available data before September 2014. On the other hand, point R (Fig. 4b-7) located at a distance of ∼300 m from point P, as indicated by gray lines,

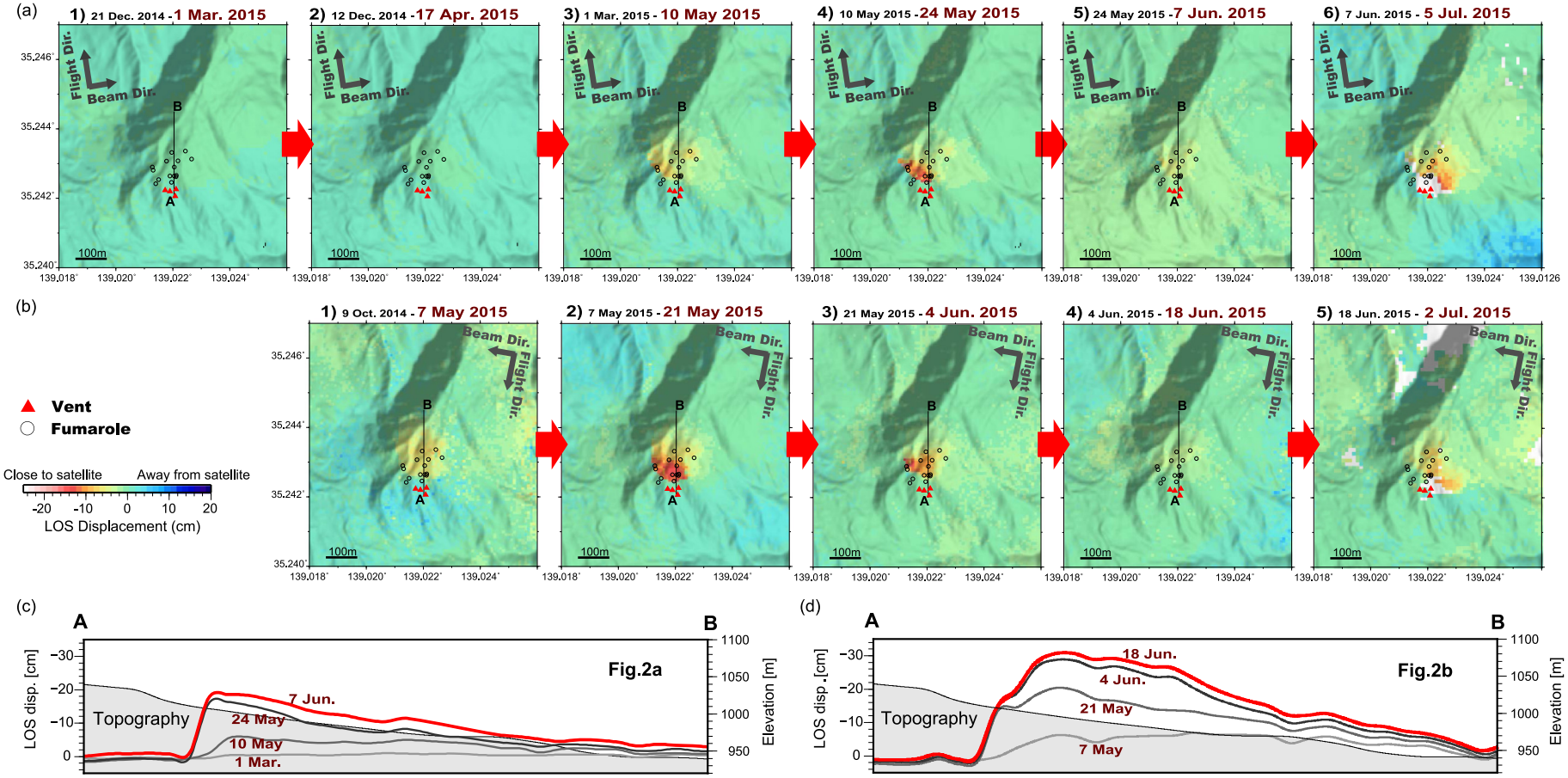

Fig. 2. Detection of locally distributed ground inflation prior to a small phreatic eruption. (a) ALOS-2 InSAR-derived ground displacements for the ascending orbit. Minus sign means a LOS shortening signal. (b) Same as Fig. 2a but for the descending orbit. (c) Cumulative displacements on the cross section A–B for the ascending orbit. (d) Same as Fig. 2c but for the descending orbit.

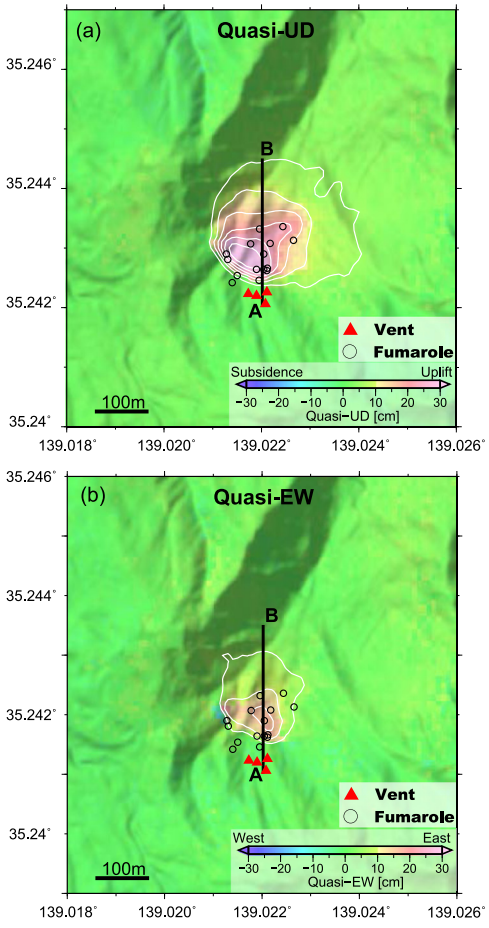

Fig. 3. Quasi-up–down (a) and quasi-east–west (b) displacements calculated by using the cumulative displacements derived from ALOS-2 data. Red triangles and open circles represent eruption vents and fumaroles, respectively. The time span for the estimate of cumulative displacement is from 1 May 2015 to 7 June 2015 for the ascending orbit data (Fig. 2a-1 to 2a-5), while for the descending orbit data the time span is from 7 May 2015 to 18 June 2015 (Fig. 2b-1 to 2b-4).

did not show any significant ground deformation. The deformation proceeded in a spatially limited area.

These findings obtained from RS2 and S1 strongly suggest that the subsurface pressure increase had already started, which was probably caused by some significant volcanic fluid and/or heat injection, prior to the enhancement of the seismic swarm activity and the GNSS-observed volcano inflation identified at the end of April 2015.

It is further noted that neither PSI analysis nor MTI analysis without applying the phase linking method could exploit any meaningful signals (Supplementary Figs. S3, S4, S5). The PSI method, which is the most standard approach to InSAR time series analysis (Ferretti et al., 2001), did not work well in non-urban areas as expected (Supplementary Fig. S3) because it was difficult to properly pick up naturally derived PSs. We also conducted a different PSI analysis implemented in StaMPS software with the default parameters (Hooper et al., 2012) (Fig. S4). The density of measurement points slightly increases, but is still much lower than that derived by our MTI approach.

We further confirmed the result obtained by SBAS method. Fig. S5 shows the LOS displacement field derived by a single-look-based SBAS analysis using a calculation command “mb_pt” implemented in GAMMA/IPTA, which functions on the basis of a method presented in Schmidt and Bürgmann (2003). Although the deformation is slightly identified, the spatial density of measurement points is much lower than that derived from our MTI approach.

Supplementary Fig. S6 shows the velocity field and the time history of InSAR data obtained in the same manner as Fig. 4 but without applying the phase linking method. The plotted measurement points are the same as those of Fig. 3. We could hardly exploit any meaningful signals from these InSAR images. On the other hand, through phase optimization processing, we were able to successfully exploit much more high-measurement accuracy pixels compared to conventional approaches, such as PSI (Ferretti et al., 2001), while keeping the original pixel spacing even in non-urban areas. Further we partly succeeded in measuring the displacement robustly even for the vegetation-covered areas; e.g., point R and the surroundings (aerial photo in Fig. 1a). This advanced technique was able to successfully unveil the slowly progressing local ground deformation. Here, we emphasize that the phase optimization for DSs effectively worked to detect the inflational deformation even for C-band SAR data in the mountainous area.

4. Discussion

4.1. Pressure source model

Volcanic hydrothermal systems, which commonly develop within the shallow levels of volcanic edifices (e.g., Wright et al., 1985; Pellerin et al., 1996), are thought to be intimately involved with phreatic eruptions (Ussher et al., 2000; Kanda et al., 2010; Seki et al., 2015). Fluid-rich sources confined by less permeable clay-rich sediments often lie horizontally within these areas and take on a convex lens-shape (Seki et al., 2015; Montanaro et al., 2016). If a geothermal fluid source lay at ∼100 m in depth (Seki et al., 2015), the ground deformation could be approximately described by the elastic behavior of a fluid-saturated medium (Ingebritsen et al., 2006).

We constructed a pressure source model to account for the RS2-derived local deformation in the Owakudani geothermal area (Fig. 4). Here, we apply the penny-shaped crack model proposed by Fialko et al. (2001) (see Supplementary information in more detail). The source was obviously positioned at a shallow depth, and thus, the surrounding medium should have been soft. In this calculation, we assigned a rigidity value of 0.1 GPa with a Poisson’s ratio of 0.4 assuming fluid-saturated clay for the medium (Bowles, 1996). The pressure source was eventually estimated to be located at a depth of ∼150 m from the ground surface with a pressure change of 0.7 MPa, which is equivalent to 1,330 m^3 in volume change (Table 1). The model can account for the observation with a residual of less than ∼1 cm (Fig. 6).

Here, we discuss the cause of inflation by a simple analytical approach assuming that a penny-shaped circular crack filled with water exists under the ground. First, we assume that the crack bulges as a result of the direct injection of liquid water. The injected volume of water can be estimated using formulation (A.3 in Supplementary information). Here, we assume a crack with an aspect ratio A of 0.1. Taking 1 GPa as the bulk modulus of water K_f (e.g., Germanovich and Lowell, 1995) and 0.1 GPa for μ as used in the pressure source modeling, the injected volume ΔV resultantly approaches to the volume change ΔV_0, that is, 1,330 m^3 (Table 1).

We next account for the inflation as the thermal expansion of liquid water confined in the circular crack. We basically followed the idea of Germanovich and Lowell (1995), but we did not take the horizontal growth of the crack into account for simplicity. By using this formulation (A.5 in Supplementary information) and taking 10^{-3}/°C as the coefficient of thermal expansion of water α_f, we derived 18 °C as the temperature increase. Here, we used the same values for the parameters of A, K_f, and μ as previous estimates. Assuming a crack with an aspect ratio of 0.1, the modeled crack bulge can be accounted for by water injection in the amount

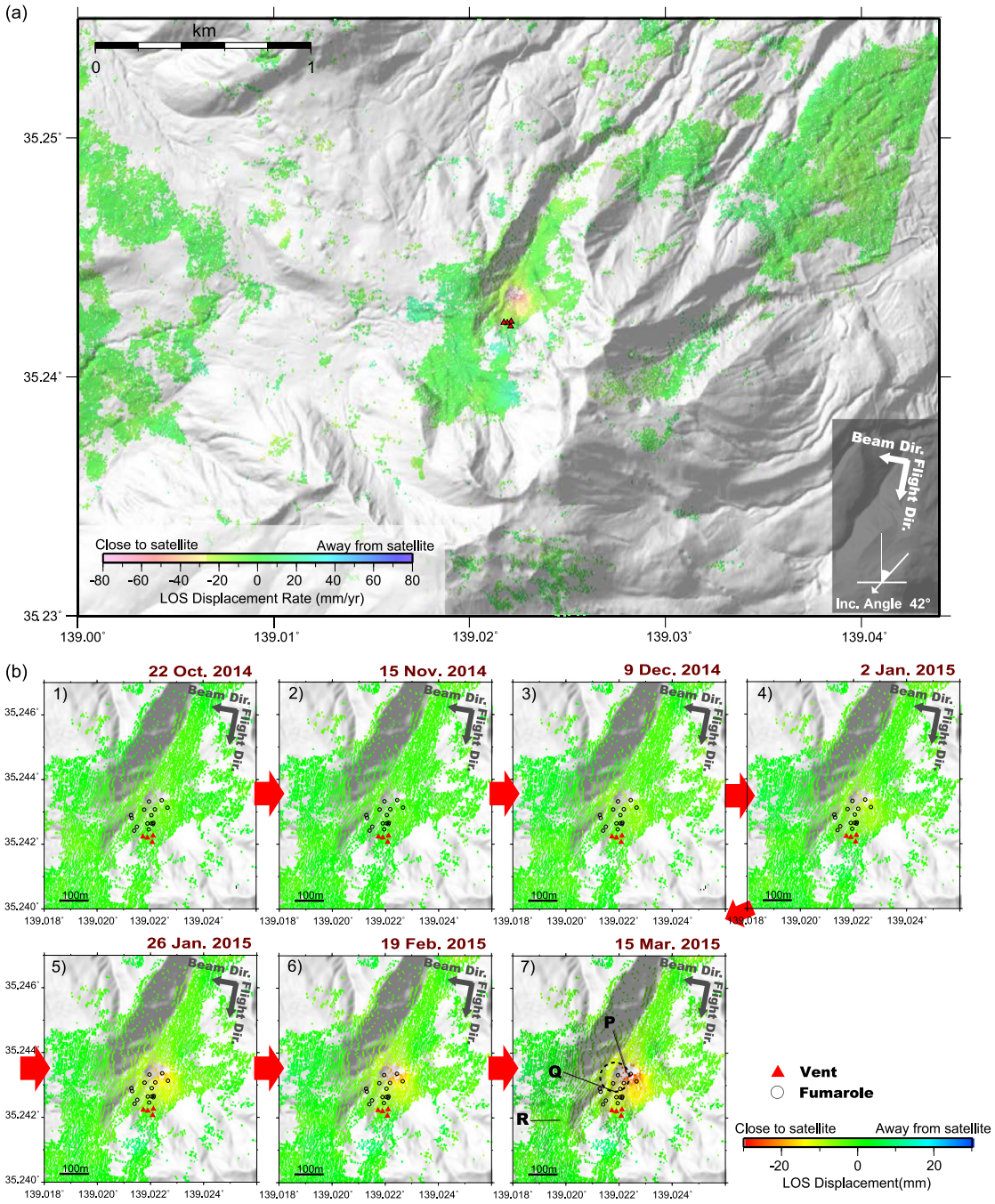

Fig. 4. RS2-detected locally distributed ground inflation since the middle of 2014. (a) Deformation velocity map from 28 September 2014 to 15 March 2015. (b) A series of InSAR images derived from MTI analysis. Dotted circle in Fig. 4b-7 indicates the horizontal position of the estimated crack bulge.

of 1,330 m^3 or a temperature increase of 18 °C. Although, in the real process, both physical processes could have contributed to the pressure increase with more complexity, the estimated fluid/heat supply seems to be within a realistic range.

4.2. Subsurface hydrothermal activity driven by deep magma behavior

Here, we will discuss the phreatic eruption in relation to the GNSS-observed inflation that likely was associated with the heat/volcanic fluid supply to the hydrothermal system. First, we modeled the inflational deformation sources for the widely distributed deformation obtained by GNSS data (black arrows in Fig. 1a). For the modeling, we assumed a combination of one spherical source (Mogi, 1958) and one opening dike (Okada, 1985) as one of the possible deformation sources. We assumed a dike source that runs nearly in the NS direction on the basis of the hypocenters, which were distributed with a NS-oriented linear trend (Fig. 1). In addition to the dike, a spherical source is essential to account for the GNSS data. This is because the site of MHAK shows significant southward movement, which cannot be produced by the NS-striking dike opening. The need for a spherical source has been proposed to explain the ground movement at MHAK in previous studies (Daita et al., 2009; Yukutake et al., 2016). The more detailed modeling approach is described in Supplementary information. The pressure sources for the GNSS-observed volcano inflation can be eventually modeled as a combination of spherical source inflation and a NS-trending dike opening (Fig. 1a and Supplementary Table S4). The spherical source may correspond to

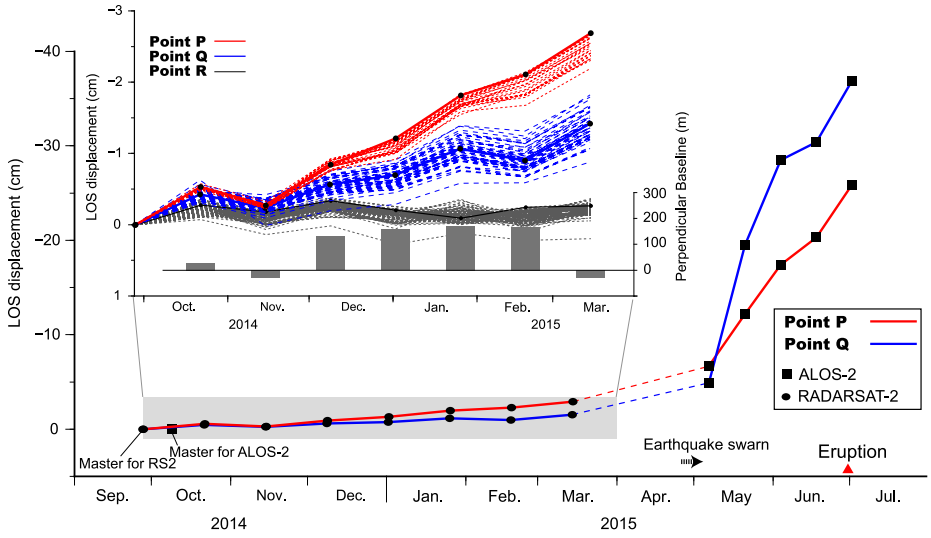

Fig. 5. Time histories of ground deformation. Red and blue lines show the time series data for the central (point P) and the southern (point Q) parts of the deformed area (Fig. 4b-7), respectively. Circles and squares represent the data acquisition dates for the RS2 and ALOS-2 satellites, respectively. The inset shows an enlarged view of the RS2-derived time histories. Dotted lines indicate the data for the surrounding points within five pixels. Vertical gray bars represent perpendicular baselines.

Table 1
Model parameters for a bulge of a penny-shaped crack. ΔP and ΔV_0 represent the internal pressure change and volume change, respectively. The depth was measured from the ground surface.

Longitude	Latitude	Depth (m)	Radius (m)	ΔP (MPa)	ΔV_0 (m^3)
139.02185 (0.00005)	35.24327 (0.00006)	152 (26)	50 (22)	0.67 (0.2)	1,330 (162)

the main magma chamber of the Hakone volcano, and the OWK geothermal area is located at the northern tip of the dike opening, which is connected to the spherical source. This implies that heat/fluid was supplied from the magma chamber beneath Mt. Komagatake via the dike-shaped passage (Fig. 7). Although OWK is located at a distance of ~6 km away from the magma chamber, it is supposed that the passage is plausible. This is because there was a good temporal correlation with the deep magma activity; the local inflation accelerated in May 2015 in synchrony with the active seismicity and volcano inflation, whereas, in June, the local deformation decelerated as the seismicity and inflation calmed down (Fig. 1b and Fig. 2). By modeling the deformation sources for the acceleration and deceleration periods, the contribution of the spherical source inflation was estimated to have decreased by ~60% in terms of the volume change per day, which may imply that the heat and/or volcanic fluid supply also decreased (Supplementary Fig. S8 and Supplementary Tables S5 and S6). The details for the modeling is described in Supplementary information. The synchronization with GNSS-observed inflation speed strongly suggests that the passage connecting the spherical source under Mt. Komagatake and the subsurface hydrothermal system at OWK has been robustly established so that heat and/or volcanic fluid can be smoothly injected to the shallow part with no substantial time delay.

As mentioned above, by viewing the time histories of GNSS data in more detail, we found that the baseline slightly lengthened starting around the time of August 2014 (Fig. 1b). This may suggest that deeply existing magma enhanced its activity one year before the eruption, and the path through which heat/fluid can ascend from the depths had already developed before April 2015. The Hakone volcano experienced several similar events consisting of volcanic activities with intense NS-trending seismic swarms and volcano inflation in 2001, 2006, 2008–2009, and 2012–2013 (Fig. 1b) (Daita et al., 2009; Yukutake et al., 2015, 2016), although these events did not lead to an eruption. The repetitive magma penetrations for over a decade might have built up a robust dike-shaped passage leading to the crust under the OWK geothermal

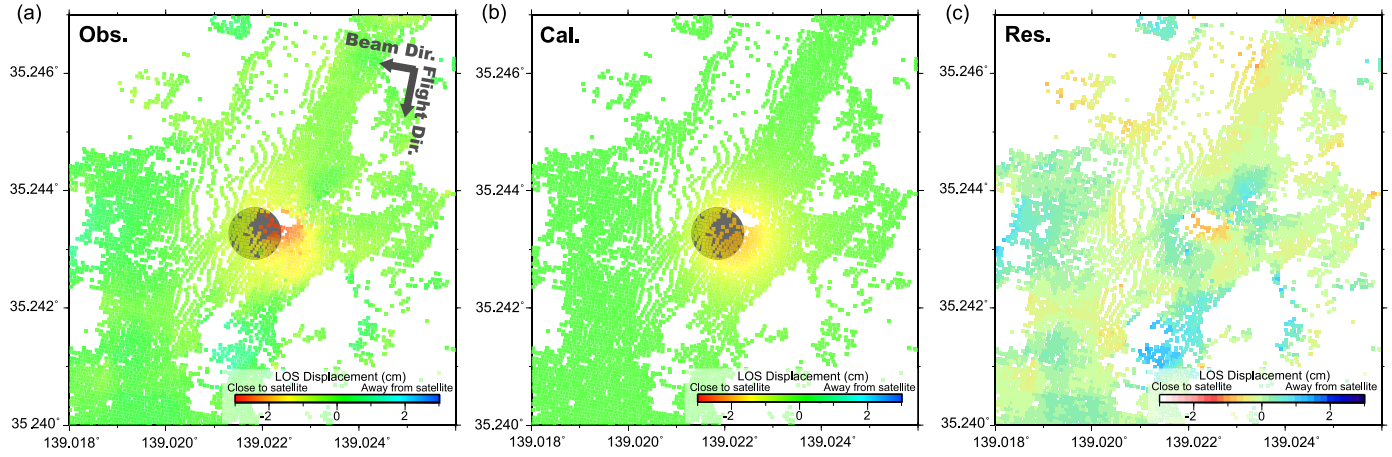

Fig. 6. Data fitting for modeling using a penny-shaped crack. (a), (b) and (c) observation, calculation, and residual, respectively. The shaded circle is the position of the estimated circular crack model. The LOS displacements from 28 September 2014 to 15 March 2015 (Fig. 4b-7) derived from RS2 are used for the estimate.

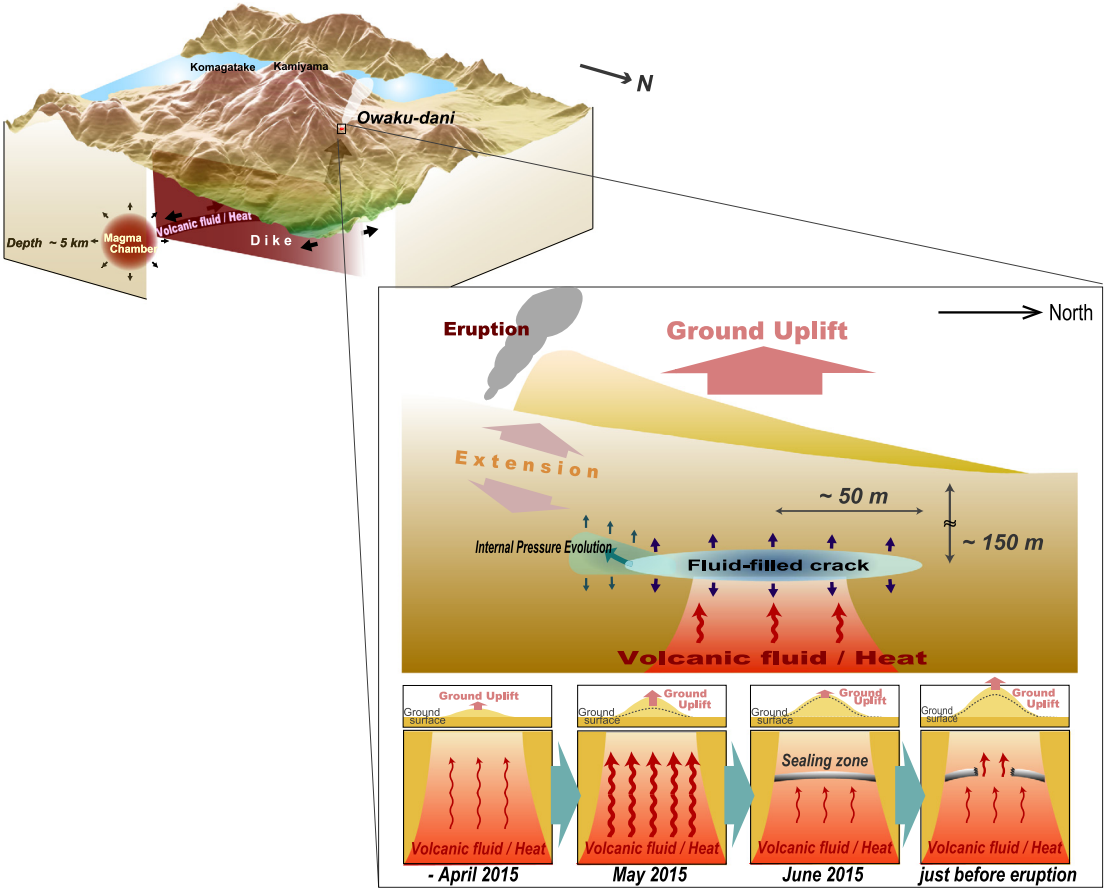

Fig. 7. Schematic view of the small phreatic eruption process and plumbing system.

area, and the subsurface hydrothermal system might thus effectively react to even slight activation of deep magma.

The local deformation in OWK decelerated in synchrony with the inactivation of the inflation of the spherical pressure source in June 2015 (Fig. 2a-5, 2b-4), followed by the eruption, which seems to present a paradoxical time evolution. However, the internal pressure in the hydrothermal system should have built up again in some way resulting in the pressure exceeding the strength of the surrounding rock. So how did the hydrothermal system recover the internal pressure while the deep magma activity calmed down? The idea of mineralogical conduit sealing, which is one of several possible mechanisms for phreatic eruptions, may give some hints for the proper interpretation (Hurst et al., 1991; Christenson et al., 2010). In analogy with it, we may interpret the following speculative scenario just before the eruption (Fig. 7). Native sulfur and/or hydrothermal minerals ascending from the depths reacted with water and deposited in the conduit, which resulted in the sealing of the conduit. However, the supply from the depths still continued without ceasing, although its rate decreased, and hence, the internal pressure increased around the sealing area; subsequently, the sealed zone was broken. The volcanic fluid and/or heat was then injected to the subsurface part once again, which caused the internal pressure to increase in bulk and eventually resulted in an eruption.

5. Conclusion

We applied standard InSAR, advanced MTI, and GNSS data analyses to the 2015 Hakone-Owakudani volcanic activity, Japan, and investigated the local ground deformation before phreatic eruptions at and around the eruption points. Our main findings are as follows:

1) We successfully detected the locally distributed ground inflation prior to the phreatic eruption where the eruption started. This is the first detection of the precursory signal, as far as we know, of which we mapped the spatial extent and its time evolution. Our finding demonstrates that the GNSS could see the deformation but could not clearly see the precursor.

2) The ground inflation proceeded at constant slow speed of ~5 mm/month in the early stage; since the end of 2014 at the latest, and then, it accelerated two months before the eruption. The ground uplift eventually reached ~30 cm.

3) The deformed area was approximately circular with a diameter of ~200 m, and the spatial extent did not change throughout the activity.

4) The maximum displacement was positioned at the center of the deformed area in the initial stage, but the peak location shifted to the southwest starting in the middle of May. The ground deformation proceeded with a trapdoor-like shape. The eruption occurred nearby the most deformed part.

5) The deformation source for the early stage can be modeled as an elastic response by a bulge of a penny-shaped crack with a pressure increase of 0.7 MPa which is embedded at the depth of ~150 m.

6) The deformation speed almost synchronized with the inflation of spherical pressure source under Mt. Komagatake, thus suggesting that heat and/or volcanic fluid supply from deep depths directly drove the subsurface hydrothermal activity.

This study demonstrates that InSAR analysis can provide a novel volcanological view for a small-sized phreatic eruption. The high-spatial-resolution SAR data unveiled the unevenly distributed

ground deformation, which was helpful for narrowing down the possible eruption point. The locally distributed ground deformation represents direct information on subsurface pressure conditions. The study demonstrates that high-spatial-resolution deformation data can be a good indicator of subsurface pressure conditions with pinpoint spatial accuracy during the preparatory process of phreatic eruptions, which may suggest that the similar signals could be detected prior to phreatic eruptions in more cases by applying the elaborated InSAR analysis. InSAR-based observations have the potential to lead to a breakthrough of geophysical monitoring for small phreatic eruptions, which may in turn lead to improved assessments of future occurrence potentials and better mitigation of related disasters.

Acknowledgements

ALOS-2 and RS2 data were provided by the Japan Aerospace Exploration Agency (JAXA) under a cooperative research contract between the Geospatial Information Authority of Japan (GSI) and JAXA, and in addition, for RS2, there was a contract between JAXA and the Canadian Space Agency (CSA). The ownership of ALOS-2 and RS2 data belongs to JAXA and the MDA Corp., respectively. S1 data are from the European Space Agency (ESA) project, and these data were downloaded from the Sentinel-1 Scientific Data Hub. Portions of the GNSS data were provided by the Japan Meteorological Agency and Hot Springs Research Institute of Kanagawa Prefecture. This study was partly supported by the Japan Society for the Promotion of Science (JSPS) KAKENHI grant program (Grant Number JP16K17797). Hypocenter data processed by the Japan Meteorological Agency (JMA) were used. We used GMT (Generic Mapping Tools) software provided by Wessel and Smith (1998) for constructing the figures. We thank the editor and two anonymous reviewers for their constructive comments.

Authors' contributions

TK produced the InSAR data, constructed pressure models, and drafted the manuscript. YM prepared the Sentinel-1A data and revised the manuscript. HM constructed a calculation code for the penny-shaped crack model and revised the manuscript. All authors read and approved the final manuscript.

Competing interests

The authors declare that they have no competing interests.

Appendix A. Supplementary material

Supplementary material related to this article can be found online at https://doi.org/10.1016/j.epsl.2018.03.041.

References

Amelung, F., Jónsson, S., Zebker, H., Segall, P., 2000. Widespread uplift and 'trapdoor' faulting on Galapagos volcanoes observed with radar interferometry. Nature 407 (6807), 993–996.

Bamler, R., Hartl, P., 1998. Synthetic aperture radar interferometry. Inverse Probl. 14, R1–R54.

Barberi, F., Bertagnini, A., Landi, P., Proncipe, C., 1992. A review on phreatic eruptions and their precursors. J. Volcanol. Geotherm. Res. 56, 231–246.

Berardino, P., Fornaro, G., Lanari, R., Sansosti, E., 2002. A new algorithm for surface deformation monitoring based on small baseline differential interferograms. IEEE Trans. Geosci. Remote Sens. 40, 2375–2383.

Bowles, J.E., 1996. Foundation Analysis and Design. McGraw-Hill International Book Company, New York.

Christenson, B.W., Reyes, A.G., Young, R., Moebis, A., Sherburn, S., Cole-Baker, J., Britten, K., 2010. Cyclic processes and factors leading to phreatic eruption events: insights from the 25 September 2007 eruption through Ruapehu Crater Lake, New Zealand. J. Volcanol. Geotherm. Res. 191, 15–32.

Coordinating Committee for Prediction of Volcanic Eruption, 2015. Report issued at the 133th meeting of the committee, 21 October 2015. http://www.data.jma.go.jp/svd/vois/data/tokyo/STOCK/kaisetsu/CCPVE/shiryo/133/133_04.pdf (in Japanese).

Curlander, J.C., McDonough, R.N., 1991. Synthetic Aperture Radar: Systems and Signal Processing. John Wiley and Sons, Hoboken.

Daita, Y., Tanada, T., Tanbo, T., Ito, H., Harada, M., Mannen, K., 2009. Temporal change of the pressure source estimated by tilt records during the 2001 Hakone swarm activity. Bull. Volcanol. Soc. Jpn. 54, 223–234 (in Japanese with English abstract).

Ferretti, A., Prati, C., Rocca, F., 2001. Permanent scatterers in SAR interferometry. IEEE Trans. Geosci. Remote Sens. 39, 8–20.

Ferretti, A., Fumagalli, A., Novali, F., Prati, C., Rocca, F., Rucci, A., 2011. A new algorithm for processing interferometric data-stacks: SqueeSAR. IEEE Trans. Geosci. Remote Sens. 49, 3460–3470.

Fialko, Y., Khazan, Y., Simons, M., 2001. Deformation due to a pressurized horizontal circular crack in an elastic half-space, with applications to volcano geodesy. Geophys. J. Int. 146, 181–190.

Fujiwara, S., Nishimura, T., Murakami, M., Nakagawa, H., Tobita, M., Rosen, P.A., 2000. 2.5-D surface deformation of M6.1 earthquake near Mt Iwate detected by SAR interferometry. Geophys. Res. Lett. 27, 2049–2052.

Fujiwara, S., Tobita, M., 1999. SAR interferometry techniques for precise surface change detection. J. Geol. Soc. Jpn. 45, 283–295 (in Japanese with English abstract).

Fujiwara, S., Tobita, M., Murakami, M., Nakagawa, H., Rosen, P.A., 1999. Baseline determination and correction of atmospheric delay induced by topography of SAR interferometry for precise surface change detection. J. Geol. Soc. Jpn. 45, 315–325 (in Japanese with English abstract).

Germanovich, L.N., Lowell, R.P., 1995. The mechanism of phreatic eruptions. J. Geophys. Res. 100, 8417–8434.

Guarnieri, A.M., Tebaldini, S., 2008. On the exploitation of targets statistics for SAR interferometry applications. IEEE Trans. Geosci. Remote Sens. 46, 3436–3443.

Handal, S., Barrios, L.A., 2004. Hydrothermal eruptions in El Salvador: a review. In: Rose, W.I., Bommer, J.J., López, D.L., Carr, M.J., Major, J.J. (Eds.), Natural Hazards in El Salvador. In: Geological Society of America Special Paper, vol. 375, pp. 245–255.

Hanssen, R.F., 2001. Radar Interferometry: Data Interpretation and Error Analysis. Kluwer Academic Publishers, Dordrecht.

Hooper, A., Bekaert, D., Spaans, K., Arikan, M., 2012. Recent advances in SAR interferometry time series analysis for measuring crustal deformation. Tectonophysics 514–517, 1–13.

Hot Springs Research Institute of Kanagawa Prefecture, Hakoneyama, 2015. Data presented at the National Committee for Prediction of Volcanic Eruption, No. 132. http://www.data.jma.go.jp/svd/vois/data/tokyo/STOCK/kaisetsu/CCPVE/shiryo/132/132_no03.pdf (accessed 22 February 2018) (in Japanese).

Hurst, A.W., Bibby, H.M., Scott, B.J., McGuinness, M.J., 1991. The heat source of Ruapehu Crater Lake; deductions from the energy and mass balances. J. Volcanol. Geotherm. Res. 46, 1–20.

Ingebritsen, S.E., Sanford, W., Neuzil, C., 2006. Groundwater in Geologic Processes. Cambridge University Press, New York.

Kanda, W., Utsugi, M., Tanaka, Y., Hashimoto, T., Fujii, I., Hasenaka, T., Shigeno, N., 2010. A heating process of Kuchi-erabu-jima volcano, Japan, as inferred from geomagnetic field variations and electrical structure. J. Volcanol. Geotherm. Res. 189, 158–171.

Kato, A., Terakawa, T., Yamanaka, Y., Maeda, Y., Horikawa, S., Matsuhiro, K., Okuda, T., 2015. Preparatory and precursory process leading up to the 2014 phreatic eruption of Mount Ontake, Japan. Earth Planets Space 67, 111.

Kobayashi, M., 1999. Tephrochronology and eruptive activity on Hakone volcano in the past 50 ka. Quat. Res. 38, 327–343 (in Japanese with English abstract).

Kobayashi, M., Mannen, K., Okuno, M., Nakamura, T., Hakamata, K., 2006. The Owakidani tephra group: a newly discovered post-magmatic eruption product of Hakone volcano, Japan. Bull. Volcanol. Soc. Jpn. 51, 245–256 (in Japanese with English abstract).

Kobayashi, T., Ishimoto, M., Tobita, M., Yarai, H., 2014. A tool for reduction of atmosphere-related noises included in an InSAR image, incorporating a numerical weather model. Bull. GSI 125, 31–38 (in Japanese).

Kobayashi, T., 2016. Effect of atmospheric-related noise reduction using numerical weather model for InSAR analysis – Application to the 2015 Sakurajima dike intrusion event. J. Geod. Soc. Jpn. 62, 79–88 (in Japanese with English abstract).

Miyaoka, K., Takagi, A., 2016. Detection of crustal deformation prior to the 2014 Mt. Ontake eruption by the stacking method. Earth Planets Space 68, 60.

Mogi, K., 1958. Relations between the eruptions of various volcanoes and the deformations of the ground surfaces around them. Bull. Earthq. Res. Inst. Univ. Tokyo 36, 99–134.

Montanaro, C., Scheu, B., Gudmunsson, M.T., Vogfjörd, K., Reynolds, H.I., Dürig, T., Strehlow, K., Rott, S., Reuschlé, T., Dingwell, D.B., 2016. Multidisciplinary constraints of hydrothermal explosions based on the 2013 Gengissig lake events, Kverkfjöll volcano, Iceland. Earth Planet. Sci. Lett. 434, 308–319.

Okada, Y., 1985. Surface deformation due to shear and tensile faults in a halfspace. Bull. Seismol. Soc. Am. 75, 1135–1154.

Pellerin, L., Johnston, J.M., Hohmann, G.W., 1996. A numerical evaluation of electromagnetic methods in geothermal exploration. Geophysics 61, 121–130.

Press, W.H., Teukolsky, S.A., Vetterling, W.T., Flannery, B.P., 1992. Numerical Recipes in Fortran77. Cambridge University Press, New York.
Schmidt, D.A., Bürgmann, R., 2003. Time dependent land uplift and subsidence in the Santa Clara Valley, California, from a large InSAR data set. J. Geophys. Res. 108, 2416.
Seki, K., Kanda, W., Ogawa, Y., Tanbo, T., Kobayashi, T., Hino, Y., Hase, H., 2015. Imaging the hydrothermal system beneath the Jigokudani valley, Tateyama, Japan: implications for structures controlling repeated phreatic eruptions from an audio-frequency magnetotelluric survey. Earth Planets Space 67, 6.
Shimkin, T., 1993. Terrestrial volcanism in space and time. Annu. Rev. Earth Planet. Sci. 21, 427–452.
Tobita, M., Fujiwara, S., Murakami, M., Nakagawa, H., Rosen, P.A., 1999. Accurate offset estimation between two SLC images for SAR interferometry. J. Geol. Soc. Jpn. 45, 297–314 (in Japanese with English abstract).
Tobita, M., 2003. Development of SAR interferometry analysis and its application to crustal deformation study. J. Geol. Soc. Jpn. 49, 1–23 (in Japanese with English abstract).
Ussher, G., Harvey, C., Johnstone, R., Anderson, E., 2000. Understanding the resistivities observed in geothermal systems. In: Proc. World Geotherm. Congr.. Kyusyu-Tohoku, Japan, pp. 1915–1920.
Yukutake, Y., Honda, R., Harada, M., Arai, R., Matsubara, M., 2015. A magma-hydrothermal system beneath Hakone volcano, central Japan, revealed by highly resolved velocity structures. J. Geophys. Res. 120, 3293–3308.
Yukutake, Y., Ueno, T., Miyaoka, K., 2016. Determination of temporal changes in seismic velocity caused by volcanic activity in and around Hakone volcano, central Japan, using ambient seismic noise records. Prog. Earth Planet. Sci. 3, 29.
Wegmüller, U., Werner, C.L., 1997. Gamma SAR processor and interferometry software. In: Proceedings of the 3rd ERS Symposium, Eur. Space Agency Spec. Publ., ESA SP-414, pp. 1686–1692.
Werner, C., Wegmüller, U., Strozzi, T., Wiesmann, A., 2003. Interferometric point target analysis for deformation mapping. In: IEEE Proceedings, International Geoscience and Remote Sensing Symposium, pp. 4362–4364.
Wessel, P., Smith, W.H., 1998. New improved version of Generic Mapping Tools released. Eos 79, 579.
Wright, P.M., Ward, S.H., Ross, H.P., West, R.C., 1985. State-of-the-art geophysical exploration for geothermal resources. Geophysics 50, 2666–2699.
Zan, D.F., Rocca, F., 2005. Coherent processing of long series of SAR images. Proc. Int. Geosci. Remote Sens. Symp., 1987–1990.